

Breather-to-soliton transitions, nonlinear wave interactions, and modulational instability in a higher-order generalized nonlinear Schrödinger equation

Lei Wang,^{1,*} Jian-Hui Zhang,² Zi-Qi Wang,² Chong Liu,³ Min Li,¹ Feng-Hua Qi,⁴ and Rui Guo⁵

¹*Department of Mathematics and Physics, North China Electric Power University, Beijing 102206, P. R. China*

²*School of Energy Power and Mechanical Engineering, North China Electric Power University, Beijing 102206, P. R. China*

³*School of Physics, Northwest University, Xi'an 710069, P. R. China*

⁴*School of Information, Beijing Wuzi University, Beijing 101149, P. R. China*

⁵*School of Mathematics, Taiyuan University of Technology, Taiyuan 030024, P. R. China*

(Received 26 September 2015; revised manuscript received 20 December 2015; published 22 January 2016)

We study the nonlinear waves on constant backgrounds of the higher-order generalized nonlinear Schrödinger (HG-NLS) equation describing the propagation of ultrashort optical pulse in optical fibers. We derive the breather, rogue wave, and semirational solutions of the HG-NLS equation. Our results show that these three types of solutions can be converted into the nonpulsating soliton solutions. In particular, we present the explicit conditions for the transitions between breathers and solitons with different structures. Further, we investigate the characteristics of the collisions between the soliton and breathers. Especially, based on the semirational solutions of the HG-NLS equation, we display the novel interactions between the rogue waves and other nonlinear waves. In addition, we reveal the explicit relation between the transition and the distribution characteristics of the modulation instability growth rate.

DOI: [10.1103/PhysRevE.93.012214](https://doi.org/10.1103/PhysRevE.93.012214)

I. INTRODUCTION

Soliton, breather, and rogue wave are three types of nonlinear waves existing in various physical fields. The temporal optical solitons have been widely investigated due to their potential applications in the long-distance optical fiber communication and all-optical ultrafast switching devices [1,2]. Rogue waves, initially termed to describe the extreme wave events that emerge in deep oceans [3], also have been extensively concerned both in experimental observations and theoretical predictions. In addition, these extreme wave events were observed in such areas as nonlinear fiber optics [4,5], Bose-Einstein condensations (BECs) [6,7], plasmas [8], and even finance [9]. Rogue waves, which have a peak amplitude generally more than twice the significant wave height, appear from nowhere and disappear without a trace [10]. Although their fundamental origins have not been explored quite clearly, there has been a consensus that rogue waves can be intimately associated with certain types of breathers of the underlying evolution equations [11–13]. Breathers serving as the potential prototypes for the rogue waves in various fields of physics develop owing to the instability of small amplitude perturbations that may grow in size to disastrous proportions [14]. There are, generally speaking, two types of breather structures, namely, the Akhmediev breather (AB) [15] and the Kuznetsov-Ma breather (KMB) [16]. The AB is a space periodic wave that is localized in time, while the KMB is localized in space and periodic in time. In certain limit cases, they both become the Peregrine soliton solution of the nonlinear Schrödinger (NLS) equation, and can be also regarded as two potential prototypes to explain the dynamics of rogue waves in a series of fields of physics. In addition, rogue waves are not limited to the solutions of 1D NLS systems. As examined in Ref. [17], some analogs

can be observed as the self-focusing or filamentary ultrafast pulses undergoing diffraction, full chromatic dispersion, Kerr and plasma nonlinearities, self-steepening, and modulational instability (MI).

Recent studies have reported the intricate relation between the soliton and breather (or rogue wave) solutions of such generalized nonlinear models as the Hirota equation [18,19], fifth-order NLS equation [20], and coupled Hirota equations [21]. As mentioned in Ref. [22], one has to assume that the perturbed field quantities are of order $\varepsilon^{\frac{1}{2}}$ (instead of ε as in the NLS equation), which leads to the need to take certain additional terms into account. In this case, one obtains the generalized NLS equation that can be converted into the Raman-extended derivative NLS (R-EDNLS) equation [23,24]. The applications of ultrashort pulses (USPs) can enhance the information capacity in the optical fiber and the higher-order effects should be considered in the corresponding mathematical models. For example, (1) it is necessary to consider the fourth-order dispersion (FOD) when the pulse width is below 10 fs [25]; (2) the higher-order nonlinearities should not be ignored when the optical field frequency approaches a resonant frequency of the optical fibers material [1,26]; (3) the self-steepening (SS) and self-frequency shift (SFS) should be added when extremely narrow pulse has very high optical intensity as the FOD and cubic-quintic nonlinearities being considered [26,27]. N. Akhmediev *et al.* have indicated that the breather solutions of the Hirota [19] and fifth-order NLS [20] equations can be converted into soliton solutions on a nonzero background. Liu *et al.* have investigated the state transition between the Peregrine soliton and W-shaped traveling wave induced by higher-order effects and background frequency [18,21]. Moreover, such transitions have also been found in certain coupled systems. For example, Wang *et al.* have discovered the elastic collision between a transformed periodic wave and a breather for the variable-coefficient NLS and Maxwell-Bloch (NLS-MB) equations [28]. In the case of the same velocity, the breather of the NLS-MB system can be

*50901924@ncepu.edu.cn

converted into various nonlinear localized and periodic waves, including multipeak soliton, periodic wave, antidark soliton, and W-shaped soliton [29].

Among various mechanisms that are related to the rogue-wave formation, the MI is the most accepted one. The pioneering work on the MI can refer to Bespalov and Talanov's study [30]. MI is a process in which the amplitude and phase modulations of a wave grow due to the interplay between the nonlinearity and dispersion [31]. The MI associated with the growth of periodic perturbations on an unstable continuous-wave background is a basic and ubiquitous nonlinear phenomenon of a large variety of nonlinear dispersive models [32]. In the initial evolution of MI, sidebands within the instability spectrum experience an exponential amplification at the expense of the pump [33]. The subsequent wave dynamics shows the more complex cases, and it involves a cyclic energy exchange between multiple spectral modes [33]. In the context of fiber optics, MI originated from noise leads to a series of high-contrast peaks of random intensity, which have structures similar to ocean rogue waves [34]. The recent studies indicate that the MI demonstrates certain interesting characteristics with the additional physical effects considered, such as the higher-order dispersion and nonlinear terms [35] and cross-phase modulation [36]. For instance, Baronio *et al.* have indicated that rogue-wave formation is related to a special kind of MI, namely, the baseband MI whose bandwidth includes arbitrarily small frequencies [36]. Liu *et al.* have recently found that an intriguing transition, described by an exact explicit rational solutions of the Hirota [18] as well as the coupled Hirota equations [21], is consistent with the MI analysis that involves a MI region and a stability region in a low perturbation frequency region.

In this paper, we study the higher-order generalized NLS (HG-NLS) equation [38],

$$i q_t + q_{xx} + 2q|q|^2 + \gamma_1(q_{xxxx} + 6q_x^2 q^* + 4q|q_x|^2 + 8|q|^2 q_{xx} + 2q^2 q_{xx}^* + 6|q|^4 q) = 0. \quad (1)$$

Hereby, $q(x, t)$ denotes the complex envelope and γ_1 stands for the strength of higher-order linear and nonlinear effects. In a long-distance and high-speed optical fiber transmission system, Eq. (1) models the propagation of USP with the FOD, cubic-quintic nonlinearity, self-steepening, and self-frequency shift [39]. In addition, Eq. (1) can also describe the nonlinear spin excitations in one-dimensional isotropic biquadratic Heisenberg ferromagnetic spin with the octupole-dipole interaction [38,40–43]. Reference [43] has investigated the Painleve property, derived the Lax pair, discussed the infinite conservation laws, and obtained some soliton solutions for Eq. (1). Reference [37] has presented breathers and multisoliton solutions of Eq. (1). The rogue wave solutions of Eq. (1) have been derived via the modified Darboux transformation (mDT) in Ref. [44]. Note that the effect of quintic nonlinear term in the R-EDNLS has been revealed in detail in Refs. [23,24]. In these works, Bergé *et al.* have discussed the dynamics of localized wave collapse in the R-EDNLS equation both analytically [23] and numerically [24]. Hereby, we reveal the intricate relation between the breather and soliton solutions of Eq. (1), which involves not only the quintic nonlinearity but also some other higher-order effects

resulting from certain physical context. Furthermore, we study the interactions among different types of nonlinear waves, including breathers, rogue waves, and solitons. In addition, we reveal the explicit relation between the transition and the distribution characteristics of the MI growth rate.

The arrangement of the paper is as follows: In Sec. II, we will present the breather, rogue wave, and semirational solutions of Eq. (1). The breather-to-soliton conversions will be studied in Sec. III. The characteristics of interactions among different types of nonlinear waves will be discussed in Sec. IV. The semirational rogue wave-to-soliton conversions will be investigated in Sec. V. The link between the MI growth rate and the transition characteristic will be revealed in Sec. VI. Finally, Sec. VII will present the conclusions of this paper.

II. BREATHER, ROGUE WAVE, AND SEMIRATIONAL SOLUTIONS

In this section, we pay attention to the analytical solutions of Eq. (1). Based on the lax pair and mDT of Eq. (1), the first-order breather solution reads as [44]

$$q_B^{[1]} = \left(c + 2\beta \frac{G_B^{[1]} + i H_B^{[1]}}{D_B^{[1]}} \right) e^{i\rho}, \quad (2)$$

with

$$\begin{aligned} \rho &= a x + b t, \quad b = (a^4 - 12a^2 c^2 + 6c^4)\gamma_1 + 2c^2 - a^2, \\ G_B^{[1]} &= k_1 k_2 \cos(t V_H + x h_R) \cosh(2\chi_I) \\ &\quad - \cosh(t V_T + x h_I) \sin(2\chi_R), \\ H_B^{[1]} &= \cos(2\chi_R) \sinh(t V_T + x h_I) \\ &\quad + k_1 k_2 \sin(t V_H + x h_R) \sinh(2\chi_I), \\ D_B^{[1]} &= \cosh(t V_T + x h_I) \cosh(2\chi_I) \\ &\quad - k_1 k_2 \cos(t V_H + x h_R) \sin(2\chi_R), \\ h &= 2\sqrt{c^2 + \left(\lambda + \frac{a}{2}\right)^2} = h_R + i h_I, \quad k_1 = 1, \quad k_2 = -1, \\ d &= \gamma_1[a(a^2 - 6c^2) - 8\lambda^3 + 4a\lambda^2 \\ &\quad + (4c^2 - 2a^2)\lambda] \frac{h}{2} t + [x + (2\lambda - a)t] \frac{h}{2} \\ &= (x + \{2\lambda - a + \gamma_1[a(a^2 - 6c^2) - 8\lambda^3 + 4a\lambda^2 \\ &\quad + (4c^2 - 2a^2)\lambda]\}t) \frac{h}{2}, \\ &= [x + (d_R + i d_I)t] \frac{h}{2}, \\ \chi &= \frac{1}{2} \arccos \frac{h}{2}, \quad V_T = 2(d_R h_I + d_I h_R), \\ V_H &= 2(d_R h_R - d_I h_I). \end{aligned}$$

Further, to obtain the second-order solution, we need two complex eigenvalues, i.e., $\lambda_{2j-1} = \alpha_{2j-1} + i \beta_{2j-1}$ where $j = 1, 2$. The expression for the second-order breather solution is given as follows [44]:

$$q_B^{[2]} = q^{[0]} - 2i \frac{\Omega_1^{[2]}}{\Omega_2^{[2]}}, \quad (3)$$

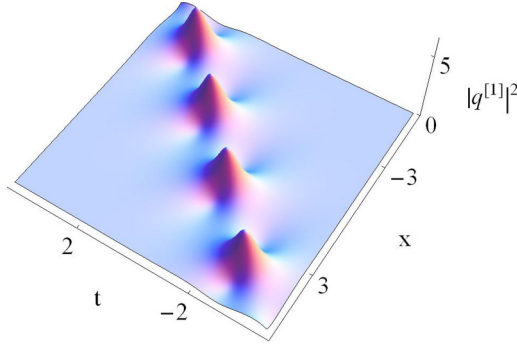


FIG. 1. First-order breather with $a = 0.5, c = 0.6, \gamma_1 = 0.1$, and $\lambda_1 = \lambda_2^* = 0.1 + 0.65i$.

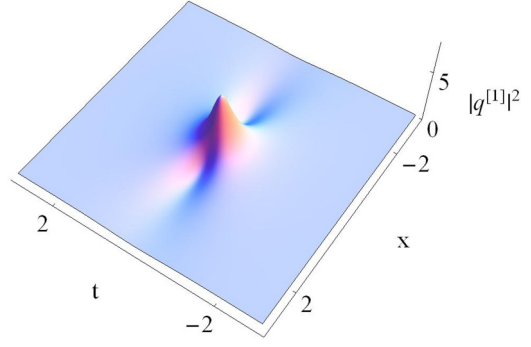


FIG. 3. First-order rogue wave with $a = 0.1, c = 0.8, \gamma_1 = 0.1$, and $\lambda_0 = -0.05 + 0.8i$.

with

$$\begin{aligned}
 q^{[0]} &= c e^{a x + b t}, \quad \lambda_1 = \lambda_2^* = \alpha_1 + \beta_1 i, \\
 \lambda_3 &= \lambda_4^* = \alpha_2 + \beta_2 i, \\
 \psi_2 &= -\varphi_1^*, \quad \varphi_2 = \psi_1^*; \quad \psi_4 = -\varphi_3^*, \quad \varphi_4 = \psi_3^*; \\
 \varphi_j &= i \frac{k_1}{c} \left(\frac{a + h_j}{2} + \lambda_j \right) e^{i(d_j + \frac{\rho}{2})} + k_2 e^{-i(d_j - \frac{\rho}{2})}, \\
 \psi_j &= k_1 e^{i(d_j - \frac{\rho}{2})} + i \frac{k_2}{c} \left(\frac{a + h_j}{2} + \lambda_j \right) e^{-i(d_j + \frac{\rho}{2})}, \\
 j &= 1, 3, \quad k_1 = -k_2 = 1, \\
 \Omega_1^{[2]} &= \begin{vmatrix} \varphi_1 & \lambda_1^2 \varphi_1 & \psi_1 & \lambda_1 \varphi_1 \\ \varphi_2 & \lambda_2^2 \varphi_2 & \psi_2 & \lambda_2 \varphi_2 \\ \varphi_3 & \lambda_3^2 \varphi_3 & \psi_3 & \lambda_3 \varphi_3 \\ \varphi_4 & \lambda_4^2 \varphi_4 & \psi_4 & \lambda_4 \varphi_4 \end{vmatrix}, \\
 \Omega_2^{[2]} &= \begin{vmatrix} \varphi_1 & \lambda_1 \psi_1 & \psi_1 & \lambda_1 \varphi_1 \\ \varphi_2 & \lambda_2 \psi_2 & \psi_2 & \lambda_2 \varphi_2 \\ \varphi_3 & \lambda_3 \psi_3 & \psi_3 & \lambda_3 \varphi_3 \\ \varphi_4 & \lambda_4 \psi_4 & \psi_4 & \lambda_4 \varphi_4 \end{vmatrix}.
 \end{aligned}$$

Figure 1 describes the first-order breather of Eq. (1). Figure 2 shows an example of the second-order breather collision, which leads to the second-order central rogue wave in the (t, x) plane. By assuming $\lambda_1 \rightarrow \lambda_0 = \alpha_0 + \beta_0 i$ and $\lambda_2 \rightarrow \lambda_0^* = \alpha_0 - \beta_0 i$ in the solution Eq. (2), Fig. 3 exhibits the first-order rogue wave of Eq. (1). It should be pointed out that

these solutions have been reported in Ref. [44]. Further, if we only let $\lambda_1 \rightarrow \lambda_0 = \alpha_0 + \beta_0 i$ and $\lambda_2 \rightarrow \lambda_0^* = \alpha_0 - \beta_0 i$ in the two-breather solution, we can obtain the semirational rogue wave solution which is depicted in Fig. 4. Such a solution is expressed in forms of the mixed rational-exponential functions and describes the nonlinear superposition of a breather with a Peregrine soliton. This diagram has also been displayed in other models, e.g., the NLS equation [14], the integrable quintic NLS equation [45], the derivative NLS equation [46], and the Lenells-Fokas equation [47]. In addition, some multicomponent systems such as the vector NLS equations [48], the wave resonant-interaction equations [49], the generalized NLS and Maxwell-Bloch equations [50], and the coupled Hirota equations [51] admit these hybrid solutions. The determinant forms of mixed rational-exponential solutions can be presented by improving the Taylor expansion technique [46,47]. Physically, they can be used to study the interactions among different types of nonlinear waves [48,49] and explain the mechanism of the higher-order rogue waves [46,47]. From Fig. 4, we observe that a second-order central rogue wave appears in the $(t-x)$ plane with $S_0 = 0$ (S_0 is the shift parameter that controls the location of the Peregrine soliton). It should be noted that the semirational solution of Eq. (1) will degenerate into that of the scalar NLS equation [14] if we set $\gamma_1 = 0$. These hybrid solutions are one way to bridge the gap between a general second-order solution and an isolated rogue wave [14].

Based on these solutions, we can implement the corresponding breather-to-soliton conversions of Eq. (1) and study

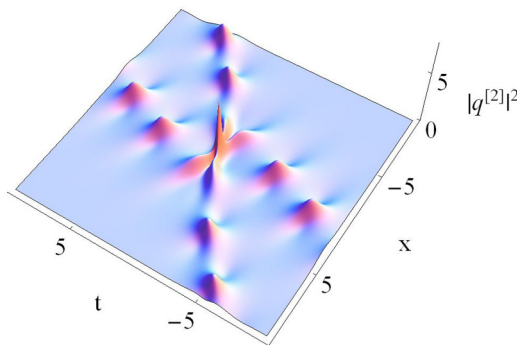


FIG. 2. Second-order breather with $a = 0.4, c = 0.4, \gamma_1 = 0.5, \lambda_1 = \lambda_2^* = 0.1 + 0.5i$, and $\lambda_3 = \lambda_4^* = 0.5i$.

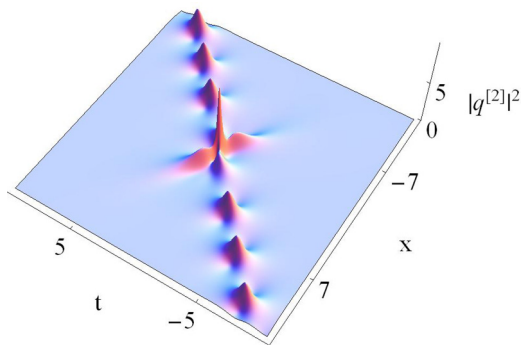


FIG. 4. Second-order semirational rogue wave with $a = 0.4, c = 0.6, \gamma_1 = 0.1, \lambda_0 = -0.2 + 0.6i$, and $\lambda_1 = \lambda_2^* = 0.1 + 0.6i$.

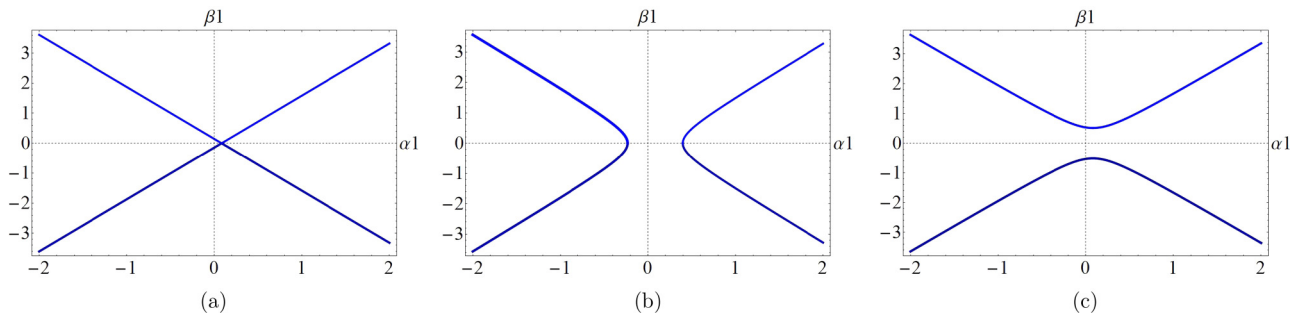


FIG. 5. Solutions of Eq. (5) on a complex plane of $\lambda = \alpha + \beta i$. (a): $a = 0.5, c = 1$, and $\gamma_1 = -\frac{6}{11}$. (b): $a = 0.5, c = 1$, and $\gamma_1 = -\frac{17}{11}$. (c): $a = 0.5, c = 1$, and $\gamma_1 = -\frac{19}{55}$.

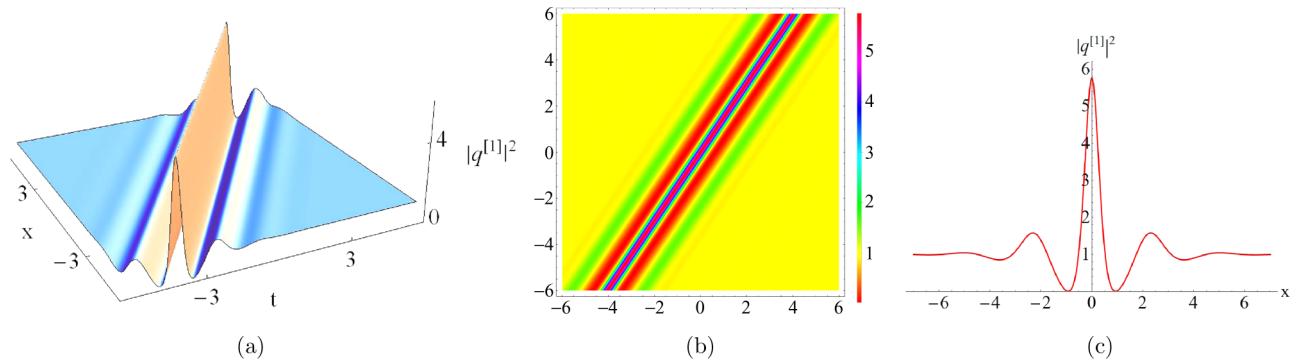


FIG. 6. A breather transformed into an oscillation W-shaped soliton with $a = 0.5, c = 1, \gamma_1 = -0.6$, and $\lambda_1 = \lambda_2^* = 0.504 + 0.7i$. (b) is the contour plot of (a). (c) is the cross-sectional view of (a) at $t = 0$.

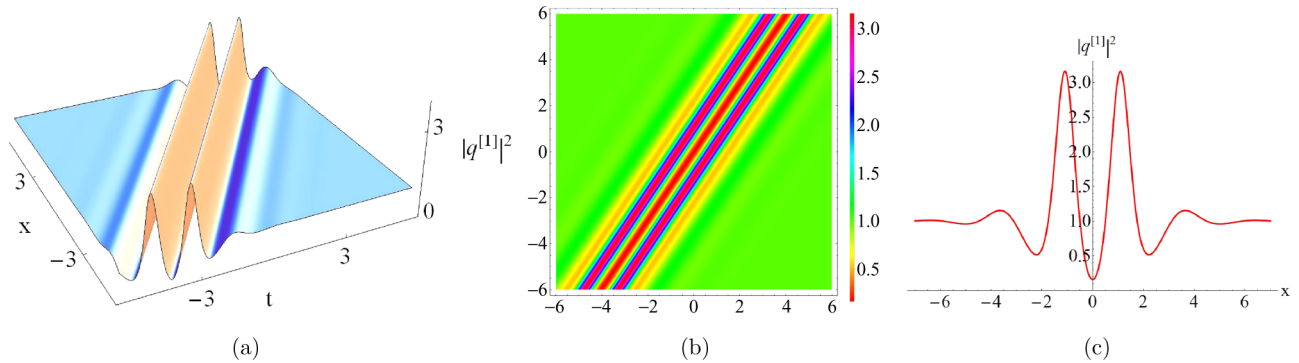


FIG. 7. A breather transformed into an oscillation M-shaped soliton with $a = 0.5, c = 1, \gamma_1 = -0.6$, and $\lambda_1 = \lambda_2^* = 0.504 - 0.7i$. (b) is the contour plot of (a). (c) is the cross-sectional view of (a) at $t = 0$.

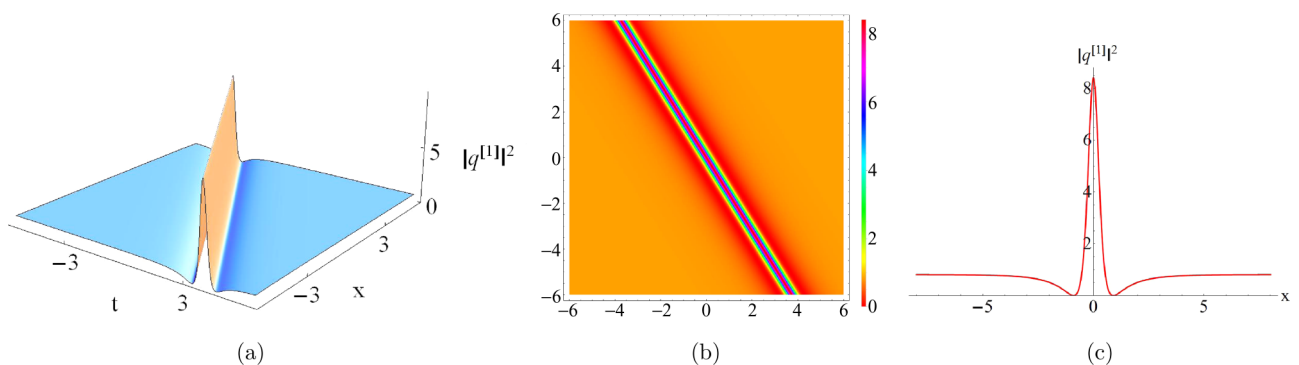


FIG. 8. A breather transformed into a W-shaped soliton with $a = 0.5, c = 0.9, \gamma_1 = -0.243$, and $\lambda_1 = \lambda_2^* = -0.25 - i$. (b) is the contour plot of (a). (c) is the cross-sectional view of (a) at $t = 0$.

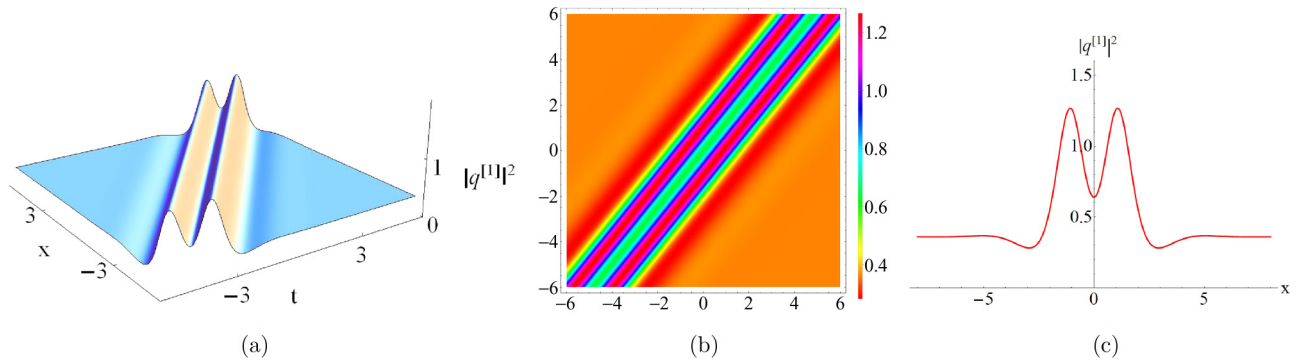


FIG. 9. A breather transformed into a M-shaped soliton with $a = 0.5$, $c = 0.6$, $\gamma_1 = -0.6$, and $\lambda_1 = \lambda_2^* = 0.349 - 0.7i$. (b) is the contour plot of (a). (c) is the cross-sectional view of (a) at $t = 0$.

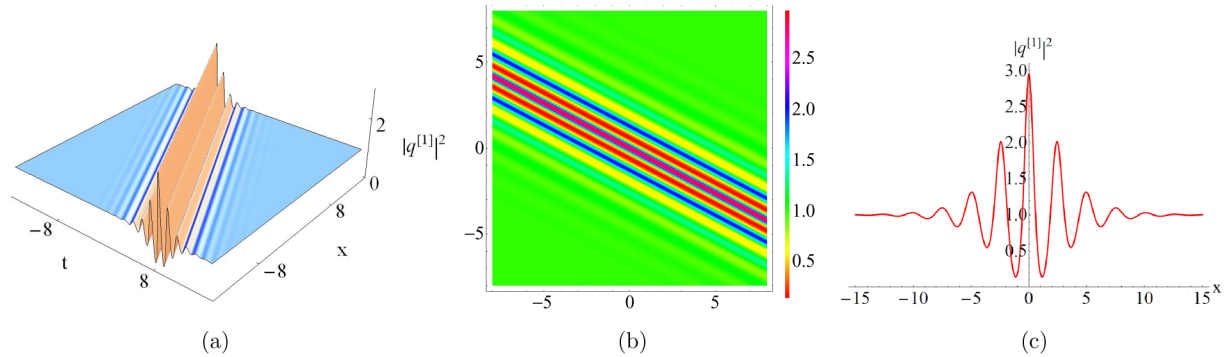


FIG. 10. A breather transformed into an oscillation W-shaped soliton with $a = 0.5$, $c = 1$, $\gamma_1 = -4.382$, and $\lambda_1 = \lambda_2^* = 0.504 + 0.36i$. (b) is the contour plot of (a). (c) is the cross-sectional view of (a) at $t = 0$.

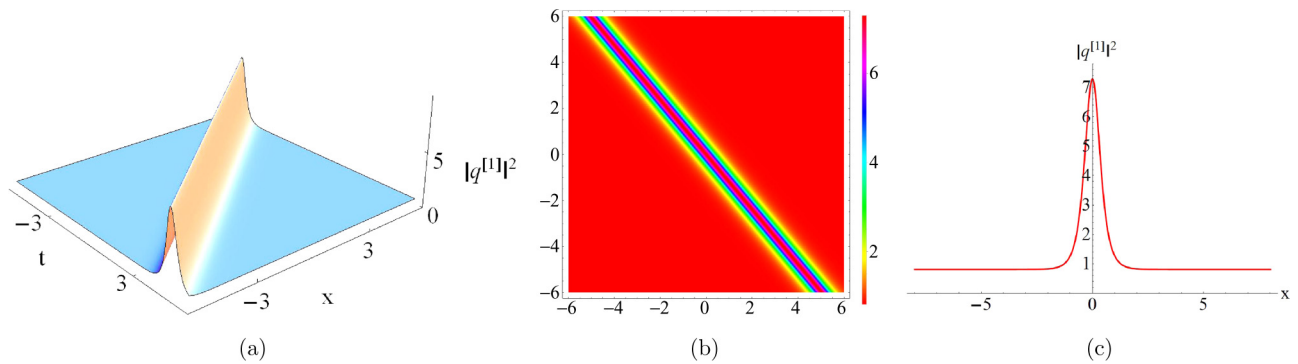


FIG. 11. A breather transformed into an antidark soliton with $a = 0.5$, $c = 0.9$, $\gamma_1 = -0.076$, and $\lambda_1 = \lambda_2^* = -0.25 + 1.8i$. (b) is the contour plot of (a). (c) is the cross-sectional view of (a) at $t = 0$.

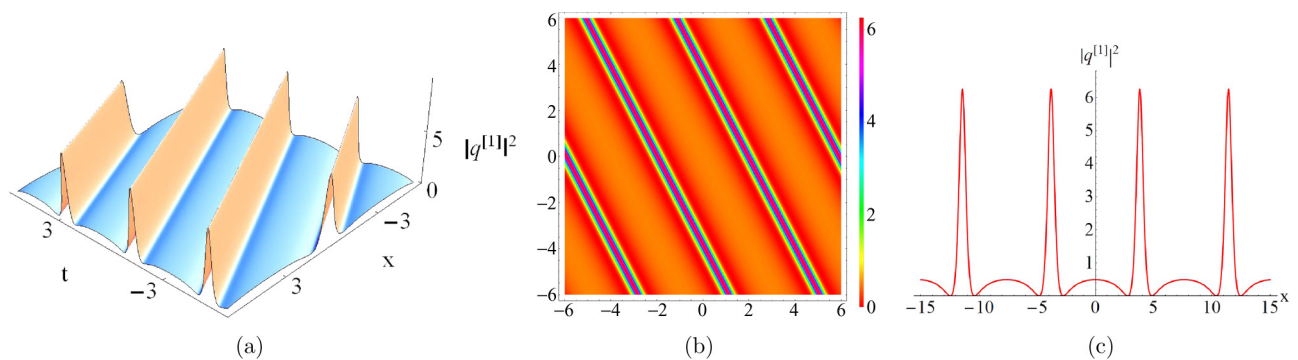


FIG. 12. A breather transformed into a periodic wave with $a = 0.5$, $c = 0.9$, $\gamma_1 = -0.373$, and $\lambda_1 = \lambda_2^* = -0.25 + 0.8i$. (b) is the contour plot of (a). (c) is the cross-sectional view of (a) at $t = 0$.

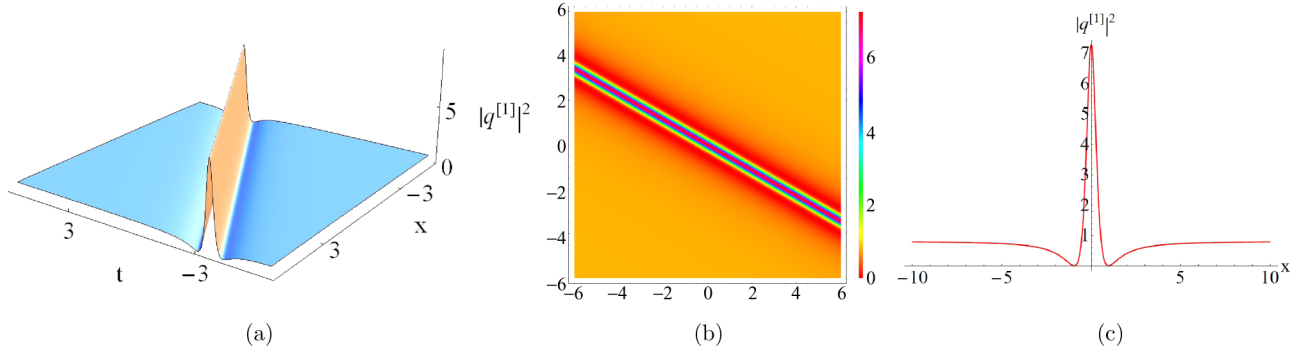


FIG. 13. A rogue wave transformed into a W-shaped soliton with $a = 0.5, c = 0.9, \gamma_1 = -0.298$, and $\lambda_0 = -0.25 + 0.9i$. (b) is the contour plot of (a). (c) is the cross-sectional view of (a) at $t = 0$.

the interactions among different nonlinear waves, including the breather, rogue wave, and soliton on nonzero backgrounds.

III. BREATHER-TO-SOLITON CONVERSIONS OF EQ. (1)

In order to explore the dynamical properties of Eq. (1), we first pay attention to the explicit expression of the solution Eq. (2). It includes the hyperbolic functions $\sinh F$ ($\cosh F$) and the trigonometric functions $\sin G$ ($\cos G$), where $d_R + \frac{d_I h_R}{h_I}$ and $d_R - \frac{d_I h_I}{h_R}$ are the corresponding velocities. In this case, the hyperbolic functions and trigonometric functions, respectively, characterize the localization and the periodicity of the transverse distribution t of those waves. The nonlinear structure described by the solution Eq. (2) can be seen as a nonlinear combination of a soliton and a periodic wave with the velocities $d_R + \frac{d_I h_R}{h_I}$ and $d_R - \frac{d_I h_I}{h_R}$. Next, we will display various nonlinear wave structures that depend on the values of velocity difference, namely, $\frac{d_I(h_R^2 + h_I^2)}{h_R h_I}$.

If the velocity difference is not equal to zero, i.e., $d_I(\frac{h_R^2 + h_I^2}{h_R h_I}) \neq 0$ (or $d_I \neq 0$), the solution Eq. (2) characterizes the localized waves with breathing behavior on a plane-wave background (i.e., the breathers and rogue waves). Further, if $\alpha = -\frac{a}{2}$, we have the ABs with $|\beta| < |c|$, the KMBs with $|\beta| > |c|$, and the Peregrine soliton with $|\beta| = |c|$. Such solutions have been derived in Ref. [44] (also see Figs. 1, 2, and 3).

Instead, if $d_I = 0$, the wave described by the solution Eq. (2) is superposed by a soliton and a periodic wave, where each has the same velocity d_R . It should be noted that the case $d_I = 0$ is equivalent to

$$\frac{V_T}{h_I} = \frac{V_H}{h_R}, \quad (4)$$

i.e.,

$$\beta^2 \gamma_1 = \frac{1}{4} (a^2 - 2c^2 - 4a\alpha + 12\alpha^2) \gamma_1 - \frac{1}{4}. \quad (5)$$

Equation (4) [i.e., Eq. (5)] implies the extrema of trigonometric and hyperbolic functions in the solution Eq. (2) is located along the same straight lines in the (x, t) plane, which leads to the transformation of the breather into a continuous soliton. Choosing different values of γ_1 in Eq. (5), we plot the curves on the α - β plane. From Fig. 5, we discover that Eq. (5) shows three types of curves. Figure 5(a) corresponds to the condition

$\gamma_1 = \gamma_0$, where

$$\gamma_0 = \frac{3}{2a^2 - 6c^2}, \quad (6)$$

and the curves of the real and imaginary parts of the eigenvalue are two intersecting lines. However, when the parameter γ_1 meets the condition $\gamma_1 < \gamma_0$ or $\gamma_1 > \gamma_0$, Fig. 5(b) or 5(c) has two branches without the intersection.

Under the transition condition Eq. (5), we display four types of conversion solitons such as the oscillation W-shaped soliton with $\beta < c$ and $\alpha > -\frac{a}{2}$ in Fig. 6, the oscillation M-shaped soliton $-\beta < c$ and $\alpha > -\frac{a}{2}$ in Fig. 7, the W-shaped soliton $-\beta > c$ and $\alpha = -\frac{a}{2}$ in Fig. 8, and the M-shaped soliton $-\beta > c$ and $\alpha > -\frac{a}{2}$ in Fig. 9. The main difference between Figs. 6 (or 7) and 8 (or 9) is that the former has the oscillatory tails. The W-shaped solitons in Figs. 6 and 7 possess a single maximum peak while M-shaped ones shown in Figs. 8 and 9 have two peaks. Additionally, in order to illustrate the effect of the value of the imaginary part of eigenvalue (β), we plot Fig. 10 where the wave profile exhibits more peaks than Fig. 6.

In order to better understand this multippeak localized structure of Eq. (1), we will extract separately the soliton and periodic wave from the mixed solution Eq. (2). Specifically, the soliton exists in isolation when h_R vanishes, while the periodic wave independently exists when h_I vanishes. Correspondingly, the analytical expressions read, for the soliton,

$$q_S^{[1]} = \left(c + 2\beta \frac{G_S^{[1]} + i H_S^{[1]}}{D_S^{[1]}} \right) e^{i\rho}, \quad (7)$$

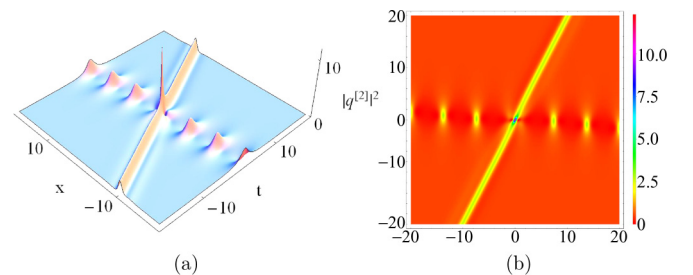


FIG. 14. Collision between a W-shaped soliton and a breather with $a = 0.3, c = 0.7, \gamma_1 = -0.257, \lambda_1 = \lambda_2^* = -0.12 + 0.5i$, and $\lambda_3 = \lambda_4^* = 0.2 + 0.9i$. (b) is the contour plot of (a).

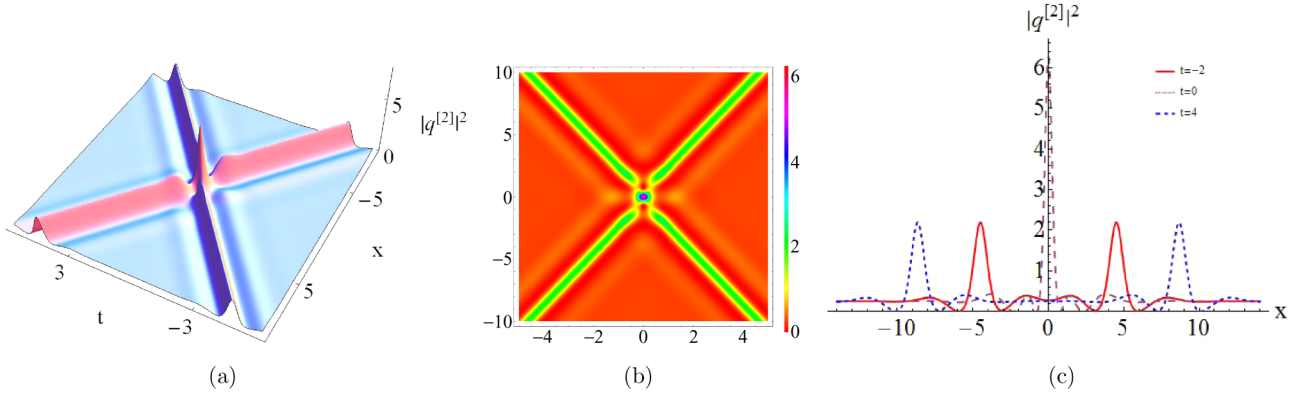


FIG. 15. Collision between two W-shaped solitons with $a = 0$, $c = 0.5$, $\gamma_1 = 0.355$, $\lambda_1 = \lambda_2^* = -0.6 + 0.5i$, and $\lambda_3 = \lambda_4^* = 0.6 + 0.5i$. (b) is the contour plot of (a). (c) is the cross-sectional view of (a).

with

$$G_S^{[1]} = \cosh(2\chi_I) - \cosh(h_I(x + 2t d_R)) \sin(2\chi_R),$$

$$H_S^{[1]} = \cos(2\chi_R) \sinh(h_I(x + 2t d_R)),$$

$$D_S^{[1]} = \cosh(h_I(x + 2t d_R)) \cosh(2\chi_I) - \sin(2\chi_R),$$

and for the periodic wave,

$$q_P^{[1]} = \left(c + 2\beta \frac{G_P^{[1]} + i H_P^{[1]}}{D_P^{[1]}} \right) e^{i\rho}, \quad (8)$$

with

$$G_P^{[1]} = \cos[h_R(x + 2t d_R)] \cosh(2\chi_I) - \sin(2\chi_R),$$

$$H_P^{[1]} = \sin[h_R(x + 2t d_R)] \sinh(2\chi_I),$$

$$D_P^{[1]} = \cosh(2\chi_I) - \cos[h_R(x + 2t d_R)] \sin(2\chi_R).$$

Figure 11 exhibits the solitary wave propagating along x direction. It is shown that this soliton lies on a plane-wave background with the peak $(c - 2\beta)^2$, which is known as the antidark soliton first reported in the scalar NLS system with the third-order dispersion [52]. Moreover, as the value of the parameter c is approaching zero, this solitary wave will turn into a standard bright soliton. Figure 12 demonstrates the periodic waves propagating in the x direction with the period $P = \frac{\pi}{h_R}$. In particular, as the period $h_R \rightarrow 0$, namely, $\beta \rightarrow c$, the periodic wave will become a single pulse with the

W-shaped structure, as depicted in Fig. 13. In this case, the solution Eq. (2) reduces to the following rational form

$$q_{RS}^{[1]} = c e^{i\rho} \left[\frac{324c^2 - 24i(18c^4 - 1)t}{c^2(4c^2(44ct + 9x)^2 + 81)} - 1 \right]. \quad (9)$$

The maximum height ($9c^2$) of the W-shaped wave is nine times the background intensity while the minimum is zero. Although this property is the same as that of the Peregrine soliton, the W-shaped wave features the soliton-like propagation properties. It should be noted that, although the structures in Figs. 8 and 13 have the similar profiles, the analytical formulas of them are different (the former expression is a mixed trigonometric and hyperbolic functions while the latter one is rational functions). In addition, we should note that the solution described by Eq. (9) can be also obtained in the order: breather \rightarrow rogue wave \rightarrow W-shaped soliton. This means that the W-shaped soliton in Fig. 13 can be derived from the rogue wave in Fig. 3 with the transition condition Eq. (5) held. The similar mechanism has been found in the Hirota and coupled Hirota equations [18,21].

IV. NONLINEAR WAVE INTERACTIONS OF EQ. (1)

In this section, we will construct the higher-order breather-to-soliton converted solutions which requires the parameters located on any of the curves in Fig. 5. For example, in

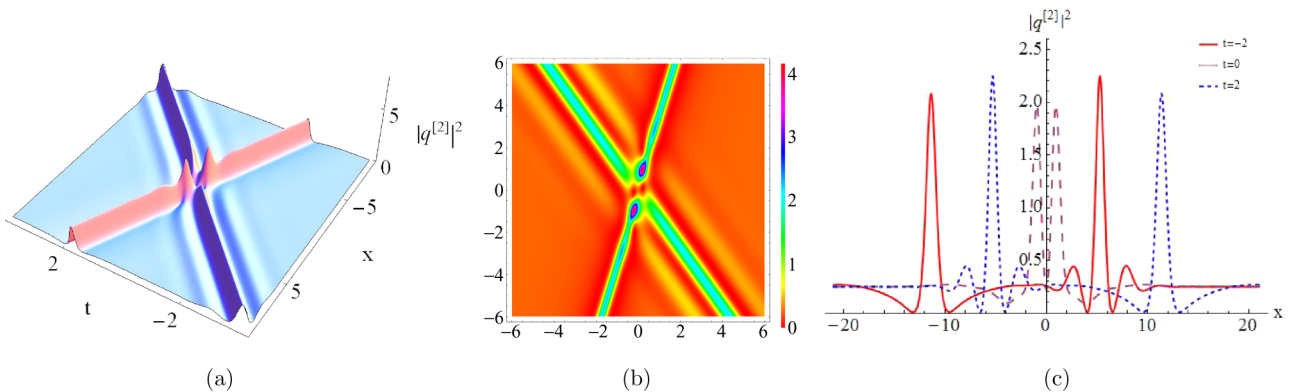


FIG. 16. Elastic collision between a W-shaped soliton and an oscillation soliton with $a = 0.7$, $c = 0.5$, $\gamma_1 = 0.613$, $\lambda_1 = \lambda_2^* = -0.37 + 0.51i$, and $\lambda_3 = \lambda_4^* = 0.6 - 0.5i$. (b) is the contour plot of (a). (c) is the cross-sectional view of (a).

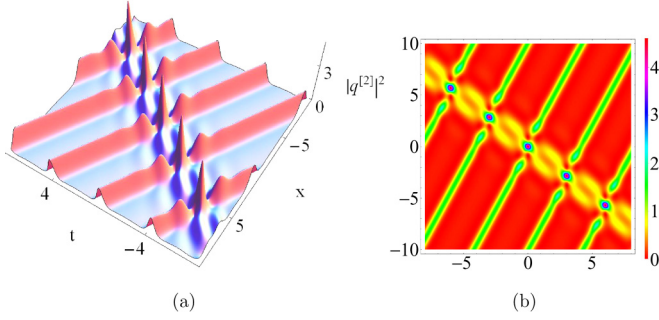


FIG. 17. Collision between a periodic wave and M-shaped solitons with $a = 0.7$, $c = 0.5$, $\gamma_1 = 0.539$, $\lambda_1 = \lambda_2^* = -0.35 + 0.382i$, and $\lambda_3 = \lambda_4^* = 0.6 + 0.44i$. (b) is the contour plot of (a).

the solution Eq. (3), we choose the parameters of one component in the two-breathers meeting Eq. (4). Therefore, the corresponding breather is converted into a soliton while another remains unchanged. Figure 14 characterizes the elastic interactions between a breather and a W-shaped soliton. Such interaction produces a higher-order rogue wave in the center as the two-breather interaction. We omit other figures describing the interactions between the breather and M-shaped soliton (or oscillation solitons) because the properties of the interactions are similar. From this figure, we find that the soliton and breather maintain their amplitudes, velocities, shapes, and period (for the breather) before and after the interaction except for the shifts. Such interactions are similar to those of the ordinary solitons of Eq. (1) [37].

On the other hand, to convert a two-breather solution into a two-soliton solution, we select all parameters in the solution Eq. (3) satisfying Eq. (4), i.e., the eigenvalues α_j and β_j ($j = 1, 2$) on the curves in Fig. 5. Several examples of two-breather collisions converted to two-soliton collisions with these eigenvalues are shown in Figs. 15 (interaction between two W-shaped solitons) and 16 (interaction between a W-shaped soliton and an oscillation W-shaped soliton). Figures 17 and 18 describe the interactions between a periodic wave and a M-shaped soliton and between a periodic wave and a W-shaped soliton, respectively. It is found that these interactions are also elastic.

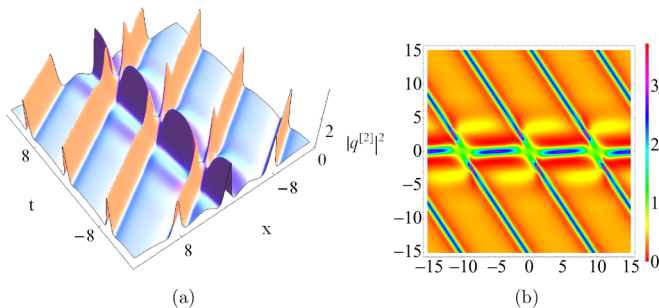


FIG. 18. Collision between a periodic wave and oscillation solitons with $a = 0.4$, $c = 0.7$, $\gamma_1 = -0.555$, $\lambda_1 = \lambda_2^* = -0.2 + 0.667i$, and $\lambda_3 = \lambda_4^* = 0.18 - 0.52i$. (b) is the contour plot of (a).

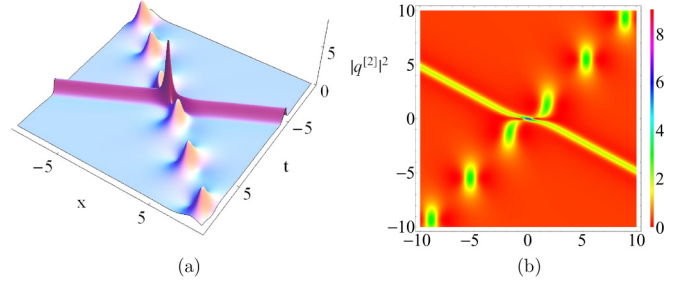


FIG. 19. Collision between a breather and a W-shaped soliton with $S_0 = 0$, $a = 0.4$, $c = 0.6$, $\gamma_1 = -0.833$, $\lambda_0 = -0.2 + 0.6i$, and $\lambda_1 = \lambda_2^* = 0.1 + 0.6i$.

V. SEMIRATIONAL ROGUE WAVE-TO-SOLITON CONVERSIONS

In this section, based on the semirational rogue wave in Fig. 4, we study the interactions between the breather and soliton, and the soliton and rogue wave. First, we consider the parameter $\lambda_0 = \alpha_0 + \beta_0 i$ in the rogue wave satisfying Eq. (4). In this case, the rogue wave is converted into a W-shaped soliton while the breather remains unchanged, as depicted in Fig. 19. The interaction is elastic as that of Fig. 14.

In Sec. II, we present the breather, rogue wave, and semirational solutions for HGNLS equation with $k_1 = 1$ and $k_2 = -1$. However, to derive different rogue-wave patterns, k_1 and k_2 are set to be arbitrary constants. Thus, we set k_1 and k_2 as following:

$$k_1 = \exp \left[-\frac{h}{4} (S_0 + S_1 \epsilon + S_2 \epsilon^2 + S_3 \epsilon^3 + \cdots + S_{k-1} \epsilon^{k-1}) \right],$$

$$k_2 = \exp \left[\frac{h}{4} (S_0 + S_1 \epsilon + S_2 \epsilon^2 + S_3 \epsilon^3 + \cdots + S_{k-1} \epsilon^{k-1}) \right]. \quad (10)$$

On the one hand, the value of the shift parameter S_0 plays an important role in the location of the first-order rogue wave [53,54]. On the other hand, we report that it can influence the interaction of nonlinear waves here. Note that the elastic collision in Fig. 19 corresponds to the case $S_0 = 0$. Instead, Fig. 20 shows the inelastic interaction between a breather and a W-shaped soliton with $S_0 = 1.5$. We note that the maximum and minimum intensities of the W-shaped soliton significantly increase after the interaction but the breather maintains its physical quantities. Our findings indicate that not only does the shift parameter S_0 control the locations of the rogue waves, but it also has the effects on the characteristics of the interactions among different nonlinear waves.

Only when the breather parameters $\lambda_1 = \lambda_2^* = \alpha_1 + \beta_1 i$ in the semirational solution satisfy Eq. (5), we can observe the interactions between the rogue waves and solitons. For example, by choosing the proper parameters, Fig. 21 displays the interaction between a W-shaped soliton and a rogue wave. It is found that the rogue wave is broken off two half when the soliton passes through it. Similarly, Fig. 22 describes the interaction between an oscillation W-shaped soliton and a rogue wave. Finally, Fig. 23 is plotted for the interaction between an antidark soliton and rogue wave. Such physical quantities as intensities, widths, shapes, and velocities of the solitons remain unchanged after the collision except for the shifts.

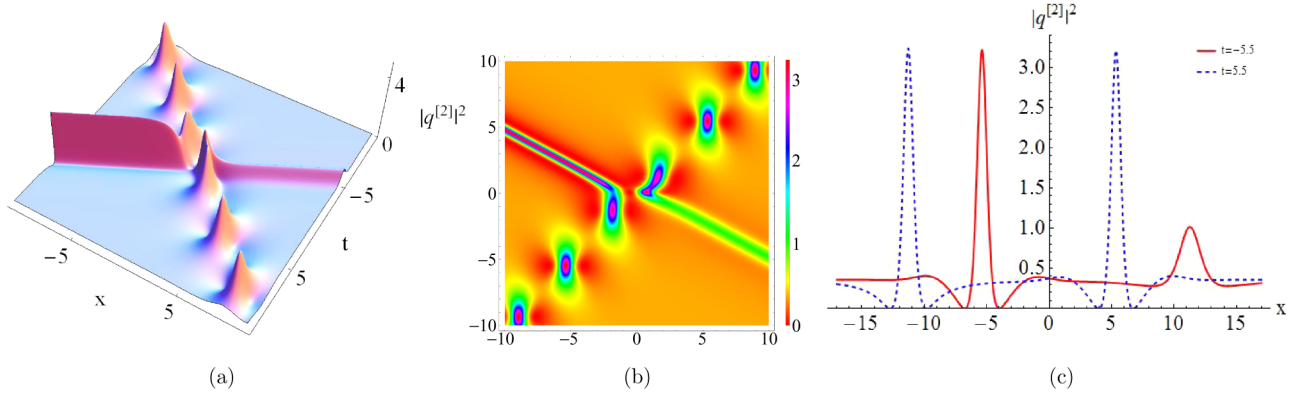


FIG. 20. Inelastic collision between a breather and a W-shaped soliton with $S_0 = 1.5$, $a = 0.4$, $c = 0.6$, $\gamma_1 = -0.833$, $\lambda_0 = -0.2 + 0.6i$, and $\lambda_1 = \lambda_2^* = 0.1 + 0.6i$.

VI. MI CHARACTERISTICS

We establish the explicit relation between the transition and the distribution characteristics of the MI growth rate for Eq. (1) in this section. Based on the method of investigating the MI of the NLS equation [1], we hereby perform a linear stability analysis of the plane-wave solution. It is easy to find that Eq. (1) admits the plane-wave solution as

$$q(x,t) = c e^{i(ax+bt)}, \quad (11)$$

where c , a , and b are real parameters, and substitution of the perturbation solution,

$$q(x,t) = [c + \epsilon \hat{q}(x,t)] e^{i(ax+bt)}, \quad (12)$$

into Eq. (1) yields the evolution equation for the perturbation as

$$\begin{aligned} & 2c^2 \hat{q}(x,t) - 12a^2 c^2 \gamma_1 \hat{q}(x,t) + 12c^4 \gamma_1 \hat{q}(x,t) \\ & + 2c^2 \hat{q}^*(x,t) - 12c^2 a^2 \gamma_1 \hat{q}^*(x,t) + i \hat{q}^{(0,1)}(x,t) \\ & + 2i a \hat{q}^{(1,0)}(x,t) - 4i a^3 \gamma_1 \hat{q}^{(1,0)}(x,t) \\ & + 24iac^2 \gamma_1 a^2 \hat{q}^{(1,0)}(x,t) + \hat{q}^{(2,0)}(x,t) - 6a^2 \gamma_1 \hat{q}^{(2,0)}(x,t) \\ & + 8c^2 \gamma_1 \hat{q}^{(2,0)}(x,t) + 2c^2 \gamma_1 \hat{q}^{*(2,0)}(x,t) \\ & + 4i a \gamma_1 \hat{q}^{(3,0)}(x,t) + \gamma_1 \hat{q}^{(4,0)}(x,t) = 0, \end{aligned} \quad (13)$$

where the superscripts (i,j) in $\hat{q}^{(i,j)}(x,t)$ stand for the i - and j -order derivatives with respect to x and t . Noting the linearity of Eq. (13) with respect to \hat{q} , we introduce

$$\hat{q}(x,t) = U_1 e^{i(\Lambda x - \Omega t)} + V_1 e^{-i(\Lambda x - \Omega^* t)}, \quad (14)$$

which is characterized by the wave number Λ and frequency Ω . Using Eq. (14) in Eq. (13) gives a linear homogeneous system of equations for U_1 and V_1 :

$$\begin{aligned} & 2c^2 U_1 + 2c^2 V_1 - 12a^2 c^2 U_1 \gamma_1 + 12c^4 U_1 \gamma_1 - 12a^2 c^2 V_1 \gamma_1 \\ & + 12c^4 V_1 \gamma_1 - 2a U_1 \Lambda + 4a^3 U_1 \gamma_1 \Lambda \\ & - 24ac^2 U_1 \gamma_1 \Lambda - U_1 \Lambda^2 + 6a^2 U_1 \gamma_1 \Lambda^2 \\ & - 8c^2 U_1 \gamma_1 \Lambda^2 - 2c^2 V_1 \gamma_1 \Lambda^2 + U_1 \Omega = 0, \end{aligned} \quad (15)$$

$$\begin{aligned} & 2c^2 U_1 + 2c^2 V_1 - 12a^2 c^2 U_1 \gamma_1 + 12c^4 U_1 \gamma_1 - 12a^2 c^2 V_1 \gamma_1 \\ & + 12c^4 V_1 \gamma_1 + 2a V_1 \Lambda - 4a^3 V_1 \gamma_1 \Lambda + 24ac^2 V_1 \gamma_1 \Lambda \\ & - V_1 \Lambda^2 - 2c^2 U_1 \gamma_1 \Lambda^2 + 6a^2 V_1 \gamma_1 \Lambda^2 \\ & - 8c^2 V_1 \gamma_1 \Lambda^2 - V_1 \Omega = 0. \end{aligned} \quad (16)$$

From the determinant of the coefficient matrix of Eqs. (15)~(16), the dispersion relation for the linearized disturbance can be determined as

$$\Omega^2 + J_1 \Omega + J_0 = 0, \quad (17)$$

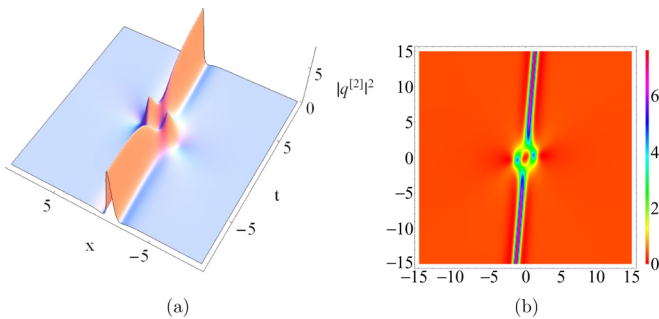


FIG. 21. Collision between a W-shaped soliton and a rogue wave with $a = 0.5$, $c = 0.6$, $\gamma_1 = -0.188$, $\lambda_0 = -0.25 + 0.6i$, and $\lambda_1 = \lambda_2^* = -1.1i$.

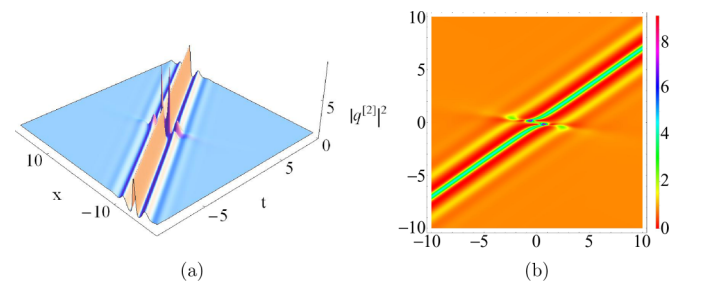


FIG. 22. Collision between an oscillation soliton and a rogue wave with $a = 0.3$, $c = 0.9$, $\gamma_1 = -0.737$, $\lambda_0 = -0.15 + 0.9i$, and $\lambda_1 = \lambda_2^* = 0.42 - 0.6i$.

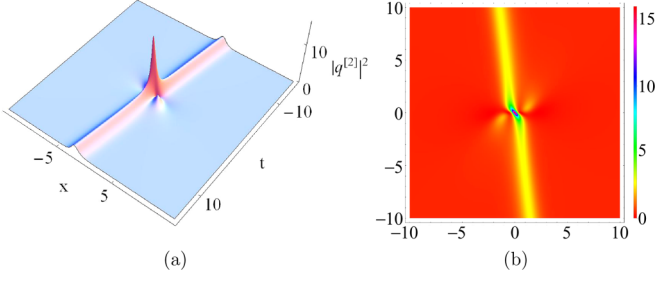


FIG. 23. Collision between an antidark soliton and a rogue wave with $a = 0.5$, $c = 0.6$, $\gamma_1 = -0.188$, $\lambda_0 = -0.25 + 0.6i$, and $\lambda_1 = \lambda_2^* = 1.1i$.

with

$$\begin{aligned} J_1 &= -4a\Lambda(4a^2\gamma_1 + 6c^2\gamma_1 + Z), \\ J_0 &= \Lambda^2(16a^6\gamma_1^2 - 4a^4\gamma_1(4 + 12c^2\gamma_1 + 9\gamma_1\Lambda^2) \\ &\quad + (Z + 6a^2\gamma_1)[24c^4\gamma_1 - \Lambda^2 + c^2(4 - 10\gamma_1\Lambda^2)] \\ &\quad + 4a^4\{1 + 3\gamma_1[24c^4\gamma_1 + \Lambda^2 + c^2(4 + 8\gamma_1\Lambda^2)]\}), \\ Z &= 1 - 6a^2\gamma_1 + 6c^2\gamma_1. \end{aligned}$$

Solving the above equation, we have

$$\begin{aligned} \Omega &= 2a\Lambda(4a^2\gamma_1 + 6c^2\gamma_1 + Z) \\ &\quad \pm \Lambda\sqrt{Z[\Lambda^2(4c^2\gamma_1 + Z) - 4Zc^2]}. \end{aligned} \quad (18)$$

In this case, the frequency Ω becomes complex and the disturbance will grow with time exponentially if and only if $\Lambda^2 < \Lambda_c^2 = \frac{4Zc^2}{4c^2\gamma_1 + Z}$, and the growth rate of the instability is given by

$$\Gamma = |\Lambda|\sqrt{Z[-\Lambda^2(4c^2\gamma_1 + Z) + 4Zc^2]}. \quad (19)$$

To obtain the maximum growth rate of the instability, we take the derivative of Eq. (19), with respect to Λ , and set it to zero. Then, in the range of $\gamma_1 > \frac{1}{6a^2 - 6c^2}$ or $\gamma_1 \leq \frac{1}{6a^2 - 10c^2}$, we obtain

$$\Lambda_{\max} = \pm\sqrt{(2c^2Z)/(4c^2\gamma_1 + Z)}. \quad (20)$$

With the above value of Λ_{\max} , we obtain the following maximum growth rate of the instability:

$$\Gamma_{\max} = \frac{2c^2|Z|}{\sqrt{1 + 4c^2\gamma_1/Z}}. \quad (21)$$

Figure 24 shows the effect of γ_1 on the maximum growth rate of the instability (Γ_{\max}) with $c = 0.9$ and $a = 0.5$. It is found that Γ_{\max} decreases with the increase of γ_1 for $\gamma_1 \leq \frac{1}{6a^2 - 10c^2}$ while it increases with the increase of γ_1 for $\gamma_1 > \frac{1}{6a^2 - 6c^2}$. In fact, γ_1 not only affects the the maximum growth rate of the instability, but also is responsible for localization of transformed solitons in the space direction.

Figure 25 shows the characteristics of MI on the (a, Λ) plane. In the case $\gamma_1 = 0$, namely, the scalar NLS equation, it is shown in Fig. 25(a) that the MI exists in the region $-2c < \Lambda < 2c$, and the distribution of the zero-frequency MI growth rate is uniform. Nevertheless, in the case $\gamma_1 \neq 0$,

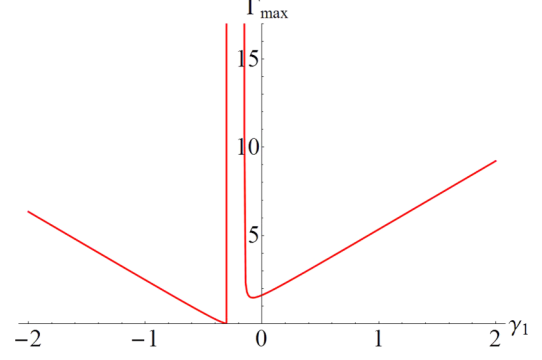


FIG. 24. The effect of γ_1 on the maximum growth rate of the instability with $c = 0.9$ and $a = 0.5$.

it is found that the higher-order effects affect the distribution characteristic of MI growth rate in the subregion $-2c < \Lambda < 2c$. Figure 25(b) contains two symmetric modulation stability (MS) regions where the corresponding MI growth rate is zero. Further, the MS regions [the dashed red lines in Fig. 24(b)] can be presented analytically,

$$a = a_s = \pm\sqrt{\frac{1}{6\gamma_1} + c^2}, \quad (22)$$

i.e.,

$$6\gamma_1 = \frac{1}{a^2 - c^2}. \quad (23)$$

The MS condition Eq. (23) includes three parameters, i.e., the higher-order effects coefficient γ_1 , the background amplitude c , and wave number a . In order to reveal the link between the MS condition Eq. (23) and transition condition Eq. (5), we need to let the eigenvalue λ approaches $\lambda_0 = -\frac{a}{2} + ic$, which is the formation condition of the rogue wave in Fig. 3. Interestingly, we discover that the MS condition Eq. (23) exactly coincides with the transition condition Eq. (5) that are required for the existence of the conversion solitons in Fig. 13. Similar to the cases of the Hirota [18] and coupled Hirota equations [21], this finding suggests that the transition between rogue waves

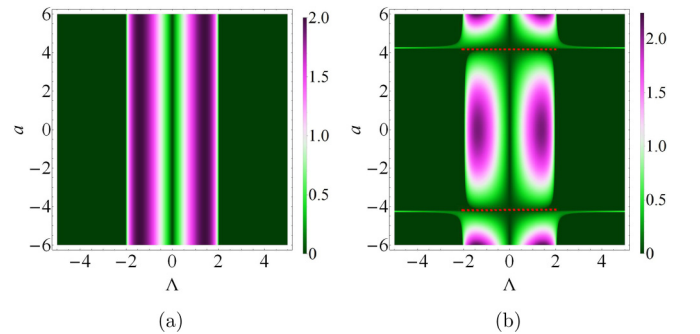


FIG. 25. Characteristics of MI growth rate Ω on (a, Λ) plane with $c=1$. (a) $\gamma_1 = 0$; (b) $\gamma_1 = 0.01$. Here the dashed red lines represent the stability region in the perturbation frequency region $-2c < \Lambda < 2c$, which is given as $a = a_s = \pm\sqrt{\frac{1}{6\gamma_1} + c^2}$.

and conversion solitons can occur in the MS region with low frequency perturbations.

VII. CONCLUSIONS

We have presented first- and second-order solutions of the HG-NLS equation and have shown that they can be converted into solitons on constant backgrounds. The condition for conversion has been explicitly presented. We have calculated the locus of eigenvalues on the complex plane which convert breathers into solitons. The solitons with these eigenvalues can collide as normal solitons on a zero background. We have provided several illustrations of such special solitons and patterns of their interactions, including the elastic and

inelastic collisions. We have also shown that this conversion is associated with the MI analysis that involves a MS region.

ACKNOWLEDGMENTS

We express our sincere thanks to all the members of our discussion group for their valuable comments. This work has been supported by the National Natural Science Foundation of China under Grants No. 11305060 and No. 61505054, by the Fundamental Research Funds of the Central Universities (Project No. 2015ZD16), by the Innovative Talents Scheme of North China Electric Power University, and by the higher-level item cultivation project of Beijing Wuzi University (Grant No. GJB20141001).

-
- [1] G. P. Agrawal, *Nonlinear Fiber Optics*, 3rd ed. (Academic Press, San Diego, CA, 2002).
- [2] A. Hasegawa and F. Tappert, *Appl. Phys. Lett.* **23**, 142 (1973); R. Radhakrishnan and M. Lakshmanan, *Phys. Rev. E* **54**, 2949 (1996); R. Radha, P. S. Vinayagam, and K. Porsezian, *ibid.* **88**, 032903 (2013).
- [3] C. Kharif and E. Pelinovsky, *Eur. J. Mech. B Fluids* **22**, 603 (2003); E. Pelinovsky and C. Kharif, *Extreme Ocean Waves* (Springer, Berlin, 2008).
- [4] J. M. Soto-Crespo, P. Grelu, and N. Akhmediev, *Phys. Rev. E* **84**, 016604 (2011).
- [5] D. R. Solli, C. Ropers, P. Koonath, and B. Jalali, *Nature* **450**, 1054 (2007); M. Erkintalo, G. Genty, and J. M. Dudley, *Opt. Lett.* **34**, 2468 (2009).
- [6] L. Wen, L. Li, Z. D. Li, S. W. Song, X. F. Zhang, and W. M. Liu, *Eur. Phys. J. D* **64**, 473 (2011).
- [7] P. S. Vinayagam, R. Radha, and K. Porsezian, *Phys. Rev. E* **88**, 042906 (2013).
- [8] W. M. Moslem, P. K. Shukla, and B. Eliasson, *Europhys. Lett.* **96**, 25002 (2011).
- [9] Z. Y. Yan, *Phys. Lett. A* **375**, 4274 (2011).
- [10] N. Akhmediev, A. Ankiewicz, and M. Taki, *Phys. Lett. A* **373**, 675 (2009).
- [11] A. Chabchoub, N. Hoffmann, M. Onorato, and N. Akhmediev, *Phys. Rev. X* **2**, 011015 (2012).
- [12] A. Chabchoub, N. P. Hoffmann, and N. Akhmediev, *Phys. Rev. Lett.* **106**, 204502 (2011).
- [13] N. Akhmediev, J. M. Soto-Crespo, and A. Ankiewicz, *Phys. Lett. A* **373**, 2137 (2009); *Phys. Rev. A* **80**, 043818 (2009).
- [14] D. J. Kedziora, A. Ankiewicz, and N. Akhmediev, *Phys. Rev. E* **85**, 066601 (2012).
- [15] N. N. Akhmediev and V. I. Korneev, *Theor. Math. Phys.* **69**, 1089 (1986).
- [16] E. A. Kuznetsov, *Dokl. Akad. Nauk SSSR* **236**, 575 (1977); Y. C. Ma, *Stud. Appl. Math.* **60**, 43 (1979).
- [17] L. Bergé, S. Mauger, and S. Skupin, *Phys. Rev. A* **81**, 013817 (2010).
- [18] C. Liu, Z. Y. Yang, L. C. Zhao, and W. L. Yang, *Phys. Rev. E* **91**, 022904 (2015).
- [19] A. Chowdury, A. Ankiewicz, and N. Akhmediev, *Proc. R. Soc. A* **471**, 20150130 (2015).
- [20] A. Chowdury, D. J. Kedziora, A. Ankiewicz, and N. Akhmediev, *Phys. Rev. E* **91**, 032928 (2015).
- [21] C. Liu, Z. Y. Yang, L. C. Zhao, and W. L. Yang, *Ann. Phys.* **362**, 130 (2015).
- [22] E. J. Parkes, *J. Phys. A: Math. Gen.* **20**, 3653 (1987).
- [23] L. Bergé, J. J. Rasmussen, and J. Wyller, *J. Phys. A: Math. Gen.* **29**, 3581 (1996).
- [24] J. S. Hesthaven, J. J. Rasmussen, L. Bergé, and J. Wyller, *J. Phys. A: Math. Gen.* **30**, 8207 (1997).
- [25] Y. Kodama and A. Hasegawa, *Solitons in Optical Communications* (Oxford University Press, Oxford, 1995).
- [26] A. I. Maimistov and A. M. Basharov, *Nonlinear Optical Waves* (Springer Press, Berlin, 1999).
- [27] M. J. Ablowitz, B. Prinari, and A. D. Trubatch, *Discrete and Continuous Nonlinear Schrödinger Systems* (Cambridge University Press, Cambridge, 2004).
- [28] L. Wang, X. Li, F. H. Qi, and L. L. Zhang, *Ann. Phys.* **359**, 97 (2015).
- [29] Y. Ren, Z. Y. Yang, C. Liu, and W. L. Yang, *Phys. Lett. A* **379**, 2291 (2015).
- [30] V. I. Bespalov and V. I. Talanov, *JETP Lett.* **3**, 307 (1966).
- [31] A. Choudhuri and K. Porsezian, *Phys. Rev. A* **85**, 033820 (2012).
- [32] V. E. Zakharov and L. A. Ostrovsky, *Physica D* **238**, 540 (2009).
- [33] F. Baronio, S. H. Chen, P. Grelu, S. Wabnitz, and M. Conforti, *Phys. Rev. A* **91**, 033804 (2015).
- [34] J. M. Dudley, F. Dias, M. Erkintalo, and G. Genty, *Nature Photon.* **8**, 755 (2014).
- [35] M. G. Forest and O. C. Wright, *Physica D* **178**, 173 (2003); L. C. Zhao, G. G. Xin, and Z. Y. Yang, *Phys. Rev. E* **90**, 022918 (2014).
- [36] F. Baronio, M. Conforti, A. Degasperis, S. Lombardo, M. Onorato, and S. Wabnitz, *Phys. Rev. Lett.* **113**, 034101 (2014).
- [37] R. Guo and H. Q. Hao, *Commun. Nonlinear Sci. Numer. Simulat.* **18**, 2426 (2013).
- [38] M. Lakshmanan, K. Porsezian, and M. Daniel, *Phys. Lett. A* **133**, 483 (1988).
- [39] T. A. Davydova and Y. A. Zaliznyak, *Physica D* **156**, 260 (2001); F. Azzouzi, H. Triki, K. Mezghiche, and A. El Akrmi, *Chaos Solitons Fractals* **39**, 1304 (2009).
- [40] S. L. Palacios and J. M. Fernández-Díaz, *Opt. Commun.* **178**, 457 (2000); M. Daniel, L. Kavitha, and R. Amuda, *Phys. Rev. B* **59**, 13774 (1999).
- [41] K. Porsezian, M. Daniel, and M. Lakshmanan, *J. Math. Phys.* **33**, 1807 (1992).
- [42] K. Porsezian, *Phys. Rev. E* **55**, 3785 (1997).

- [43] H. Q. Zhang, B. Tian, X. H. Meng, X. Lü, and W. J. Liu, *Eur. Phys. J. B* **72**, 233 (2009).
- [44] L. H. Wang, K. Porsezian, and J. S. He, *Phys. Rev. E* **87**, 053202 (2013).
- [45] A. Chowdury, D. J. Kedziora, A. Ankiewicz, and N. Akhmediev, *Phys. Rev. E* **91**, 022919 (2015).
- [46] L. Wang, Y. J. Zhu, Z. Z. Wang, F. H. Qi, and R. Guo, *Commun. Nonlinear Sci. Numer. Simulat.* **33**, 218 (2016).
- [47] L. Wang, Y. J. Zhu, F. H. Qi, M. Li, and R. Guo, *Chaos* **25**, 063111 (2015).
- [48] F. Baronio, A. Degasperis, M. Conforti, and S. Wabnitz, *Phys. Rev. Lett.* **109**, 044102 (2012); G. Mu, Z. Y. Qin, and R. Grimshaw, *SIAM J. Appl. Math.* **75**, 1 (2015).
- [49] A. Degasperis and S. Lombardo, *Phys. Rev. E* **88**, 052914 (2013).
- [50] Y. Zhang, C. Z. Li, and J. S. He, *Appl. Math. Comput.* **273**, 826 (2016).
- [51] X. Wang, B. Yang, Y. Chen, and Y. Q. Yang, *Chin. Phys. Lett.* **31**, 090201 (2014).
- [52] Y. S. Kivshar, *Phys. Rev. A* **43**, 1677(R) (1991); Y. S. Kivshar and V. V. Afanasjev, *ibid.* **44**, R1446(R) (1991).
- [53] L. J. Guo, Y. S. Zhang, S. W. Xu, Z. W. Wu, and J. S. He, *Phys. Scr.* **89**, 035501 (2013).
- [54] Y. S. Zhang, L. J. Guo, S. W. Xu, Z. W. Wu, and J. S. He, *Commun. Nonlinear Sci. Numer. Simulat.* **19**, 1706 (2014).